

Rising bubbles draw surface patterns: a numerical study

Dabao Li

School of Engineering Science, University of Chinese Academy of Sciences, Beijing 101408, China

Lang Qin and Zhigang Zuo

*State Key Laboratory of Hydrosience and Engineering,
and Department of Energy and Power Engineering,
Tsinghua University, Beijing 100084, China*

Guangzhao Zhou*

*School of Engineering Science, University of Chinese
Academy of Sciences, Beijing 101408, China, and
State Key Laboratory of Nonlinear Mechanics,
IMECH & UCAS, Beijing 100190, China*

(Dated: September 3, 2025)

Abstract

Small bubbles rising in a chain can self-organize into regular patterns upon reaching a liquid’s free surface. This phenomenon is investigated through direct numerical simulations. By varying the bubble release period, distinct branching patterns characterized by different numbers of arms are observed. These macroscopic regular configurations arise from localized non-contact repulsion and pair collisions between bubbles as they arrive at the free-surface emergence site. A theoretical model is proposed to quantitatively relate the number of branches to the bubble release period. The model also predicts probabilities of observing specific arm counts in reality. This study provides insights into broader nonlinear pattern formation and self-organization phenomena.

I. INTRODUCTION

The dynamics of gas bubbles rising in quiescent liquids have long been a fundamental topic in gas-liquid two-phase flow research[1–5]. Extensive investigations have been conducted on various aspects of single bubble behavior during ascent, including bubble morphology and terminal velocity[6–8], wake flow characteristics[9], and trajectory instability[10–12]. In practice, a probably more prevalent phenomenon is the formation of bubble chains, as commonly observed in a glass of champagne or sparkling water. In such systems, millimeter-scale bubbles are periodically generated at discrete nucleation sites located at the bottom wall of the vessels. Bubbles within a chain exhibit distinct dynamics compared to individual rising bubbles, such as a higher terminal velocity primarily due to the influence of wake flows generated by preceding bubbles[13–15]. The wake flow can also induce unsteady lift forces, which may destabilize the configuration of the bubble chain[16].

When a bubble ascends to the gas-liquid interface, it may rapidly burst, accompanied by generation of small droplets[17–20]. In cases where there are contaminants in the liquid, the bubble can float and persist for a considerable time[21]. The complexity of bubble-free surface interactions becomes more pronounced in systems that are specially designed and controlled[22, 23].

This study centers on the collective behavior of periodically-released small bubbles rising in a chain toward the free surface. After reaching the interface, the bubbles exhibit lateral migration within the horizontal plane, forming spatial patterns observed from above. While most of these patterns appear disordered, under specific conditions, the bubbles spontaneously self-organize into stable, regular configurations with rotational symmetry around the vertical ascent trajectory. An

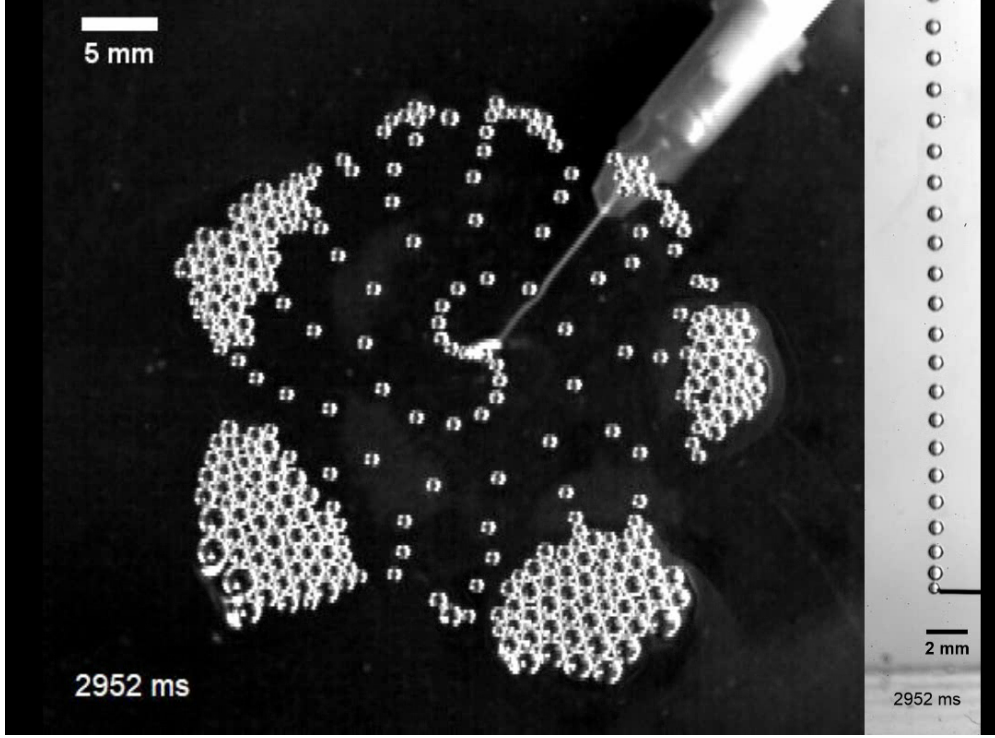


FIG. 1. Top view of the surface pattern formed by periodically injected air bubbles into a vessel partially filled with silicone oil. The image on the right is the side view of the bubble chain at the same instant.

experimental demonstration of these regular surface patterns is shown in Fig. 1. In this experiment, air bubbles with a uniform diameter of approximately 0.8 mm are periodically injected from a syringe into a vessel partially filled with silicone oil. A spiral pattern is clearly observed on the free surface when looking from above. The density, dynamic viscosity, and surface tension coefficient of the silicon oil are 935 kg/m^3 , $0.01 \text{ Pa}\cdot\text{s}$, and 0.02 N/m , respectively. The bubble release interval is 16 ms.

Despite the likelihood that such phenomenon has been observed since very early times, the literature on it is limited. The first article on this specific topic appears to be Yoshikawa *et al.* [24], where the authors conducted an experimental investigation of the surface bubble patterns as an analogy to the regular leaf arrangement in the context of phyllotaxis study (see, e.g., Ref. [25]). A phenomenological model was later developed by the same research group[26]. These two papers acknowledge the importance of bubble-bubble interactions and flow advection. Nevertheless, the mechanisms by which these factors contribute to pattern formation require further elucidation. In this paper, we revisit these regular surface patterns “drawn” by rising bubbles from a numerical perspective, aiming to gain a deeper understanding of the essential underlying mechanism of this

self-organized phenomenon.

The rest of the paper is arranged as follows: Section II describes the numerical setup of the simulations, followed by section III, where the results are presented and discussed. Section IV provides more theoretical considerations. A summary is given in section V.

II. NUMERICAL SETUP

We use the open-source software Aphros[27] for direct numerical simulations of the present two-phase flow system. Aphros solves the time-dependent incompressible Navier-Stokes equations with the divergence-free constraint, which read

$$\rho \left[\frac{\partial \mathbf{u}}{\partial t} + (\mathbf{u} \cdot \nabla) \mathbf{u} \right] = -\nabla p + \nabla \cdot \left[\mu \left(\nabla \mathbf{u} + \nabla \mathbf{u}^T \right) \right] + \mathbf{f}_\sigma + \rho \mathbf{g}, \quad (1)$$

and

$$\nabla \cdot \mathbf{u} = 0, \quad (2)$$

respectively, where \mathbf{u} is the velocity vector, p is pressure, \mathbf{g} is the gravitational acceleration, and \mathbf{f}_σ represents the surface tension effect. ρ and μ are the effective density and dynamic viscosity, respectively. They are calculated as weighted average based on the local gas volume fraction α :

$$\rho = (1 - \alpha)\rho_l + \alpha\rho_g, \quad \mu = (1 - \alpha)\mu_l + \alpha\mu_g, \quad (3)$$

where ρ_l, ρ_g, μ_l , and μ_g represent the density and viscosity of the liquid and gas phases, respectively. The evolution of α is governed by the advection equation:

$$\frac{\partial \alpha}{\partial t} + (\mathbf{u} \cdot \nabla) \alpha = 0. \quad (4)$$

Eqs. (1) and (2) are solved using the second-order Bell-Colella-Glaz method[28]. The advection of the volume fraction is handled using the volume-of-fluid (VOF) method, with a piecewise linear interface calculation (PLIC) method[29] employed for interface reconstruction. The surface tension term is defined as $\mathbf{f}_\sigma = \sigma \kappa \nabla \alpha$, where σ denotes the surface tension coefficient. The interfacial curvature, κ , is evaluated using the method of particles[30]. Additionally, an improved multi-marker technique[27] is employed in the VOF method to prevent bubble coalescence, ensuring that bubbles can float on the free surface without rupture in the simulations.

The accuracy of the solver is validated by simulating a single bubble rising in quiescent liquid. Four different liquids are tested with their physical parameters the same as those of the cases S3,

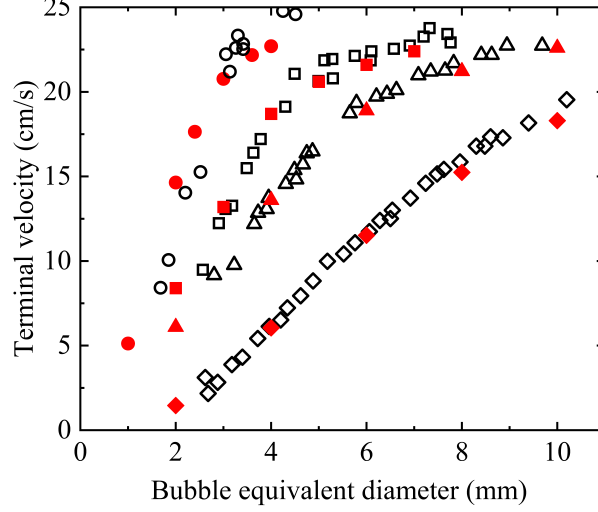


FIG. 2. Bubble's terminal rise velocity versus equivalent diameter. The black hollow symbols represent the experimental data sets S3 (diamonds), S5 (triangles), S6 (squares), and S8 (circles) from Ref. [6]. The Morton numbers for these four cases are 0.11 , 9×10^{-4} , 1×10^{-4} , and 9×10^{-7} , respectively. The red solid symbols with the same shapes are the corresponding simulation results using Aphros.

S5, S6, and S8 in Ref. [6]. The Morton numbers, defined as $Mo = g\mu_l^4/(\rho_l\sigma^3)$, are 0.11 , 9×10^{-4} , 1×10^{-4} , and 9×10^{-7} for these four cases, respectively. For each liquid, the volume-equivalent spherical diameter of the bubble, d , is varied across a relatively wide range. The computational domain is a liquid-filled box with a Cartesian mesh composed of cubic cells. The cell size is set to approximately $d/10$, maintaining consistent spatial resolution for different bubble sizes.

As can be seen in Fig. 2, the simulated terminal velocities of the bubbles (red solid symbols) show good agreement with experimental data from Ref. [6] (black hollow symbols). Notably, the terminal velocity is influenced by the deviation of the bubble shape from a sphere. Therefore, the results in Fig. 2 also demonstrate the solver's capability in capturing bubble deformation during ascent. More validation cases can be found in Ref. [27].

The computational domain for simulations of the surface patterns is a square box partially filled with liquid (see Fig. 3a). A Cartesian coordinate system is established with the origin O located at the geometric center of the box's bottom wall. The z -axis is oriented upward, while the x - and y -axes align with the side walls of the box. The dimensions of the box are $[-0.1, 0.1] \text{ m} \times [-0.1, 0.1] \text{ m} \times [0, 0.075] \text{ m}$, with the undisturbed free surface located at $z = 0.055 \text{ m}$. Gas bubbles with a volume-equivalent diameter of $d = 4 \text{ mm}$ are released periodically

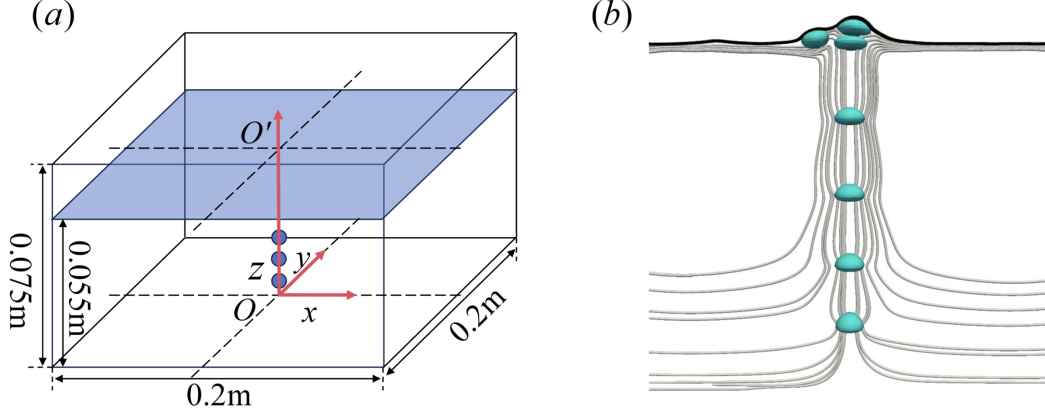


FIG. 3. (a) Illustration of the computational domain (bubble size not to scale). (b) Simulated bubbles rising in a chain, with the free surface (black) and streamlines (gray) shown in a cross-sectional view.

from a source at $(0, 0, 0.005)$ m. Free-slip conditions are imposed at the top and bottom boundaries of the computational domain, while periodic conditions are applied on all side boundaries. Since all the boundaries are reasonably far from the area of interest, i.e., the central region of the free surface, the influence of the boundary conditions on the bubble behavior is negligible. A uniform mesh with $N_x \times N_y \times N_z = 512 \times 512 \times 192$ cubic cells is used, ensuring that there are about 10 mesh cells within the diameter of a spherical bubble.

In all simulations, the gravitational acceleration is set to $g = 10 \text{ m/s}^2$ in the $-z$ direction. The liquid (l) and gas (g) phases have the following properties: $\rho_l = 1000 \text{ kg/m}^3$, $\rho_g = 30 \text{ kg/m}^3$, $\mu_l = 2 \times 10^{-2} \text{ Pa} \cdot \text{s}$, and $\mu_g = 2 \times 10^{-5} \text{ Pa} \cdot \text{s}$. The surface tension coefficient $\sigma = 0.02 \text{ N/m}$. These physical parameters are similar to those used by Yoshikawa *et al.* [24], allowing a reasonable comparison between the numerical results and the experimental data in Ref. [24]. Given the low density ratio ($\rho_g/\rho_l = 0.03$) and viscosity ratio ($\mu_g/\mu_l = 0.001$) between gas and liquid, the effects of gas phase properties are expected to be minimal. The Ohnesorge and Bond numbers are calculated as $Oh = \mu_l/\sqrt{\rho_l \sigma d} \approx 0.071$ and $Bo = \rho_l g d^2/\sigma = 8$, respectively. The corresponding Morton number is $Mo = Oh^4 Bo = 2 \times 10^{-4}$, lying between the values of cases S5 and S6 in Fig. 2. The bubbles exhibit moderate deformation during ascent. No path instabilities are observed with the parameters investigated.

For the single-bubble cases shown in Fig. 2, a bubble acquires its terminal velocity soon after release. However, because of the wake effects from preceding bubbles, for a bubble rising in a bubble chain, a much larger height is required for its velocity to reach a constant value. In the

simulations of the current study, the bubbles are still gradually accelerating before approaching the free surface. Consequently, the release depth h (or its dimensionless form h/d) might also be a relevant parameter. Nevertheless, whether the bubbles reach the terminal velocity is unlikely to have any qualitative impact on the mechanism of the pattern formation.

III. RESULTS AND DISCUSSION

A. Overview

With the VOF method, the motion and deformation of each bubble are fully resolved. Fig. 3(b) shows a cross-sectional view of the numerical result for a typical case we have simulated. The bubbles rise along a straight path in a chain and are arrested by the free surface. As can be seen from the streamlines, the bubble chain induces a vertical liquid jet along the central axis. This jet later on converts into a divergent radial flow in a thin layer beneath the free surface. Owing to the overshooting effect of the bubbles and jet, a small circular bump forms on the free surface, centered at the bubble emergence site. These observations agree well with those reported in Ref. [26].

Four representative surface patterns observed in the simulations are presented in the top panels of Fig. 4. These patterns are obtained, from (a) to (d), by decreasing the bubble release period T while keeping all other parameters fixed. Panel (a) shows a disordered mode, characterized by a random distribution of bubbles on the free surface. Panel (b) displays a two-armed mode, where the bubbles align along two branches in a straight line. Further decreasing the release period results in the multi-armed modes, as shown in panels (c) and (d). The corresponding movies for all these four cases can be found in the supplemental material of this paper.

It is known that the pattern formation is closely related to the directions in which the bubbles are emitted in sequence. In the bottom panels of Fig. 4, the difference φ (marked in Fig. 5b below, clockwise positive) in the emission direction between consecutive bubbles, referred to as the “divergence angle” in Ref. [24], is shown as a function of bubble release sequence number. As will be subsequently elucidated, φ is fully determined by the local dynamics in the vicinity of the bubble emergence site. In detail, four major mechanisms are identified to be responsible for the formation of different surface patterns. They are (i) pair collisions, (ii) non-contact repulsion, (iii) bump confinement, and (iv) flow advection. The first two mechanisms both describe the interaction between bubbles. Pair collision occurs when two bubbles are close enough with their

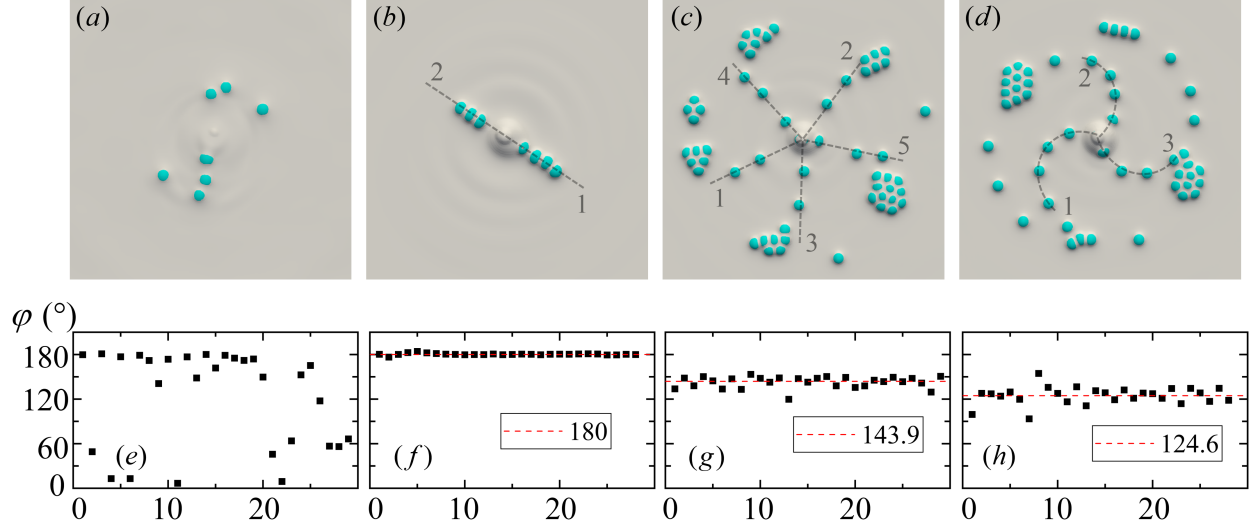


FIG. 4. (a) to (d): Four typical surface patterns observed in the numerical simulations. The dashed lines serve as visual guides to distinguish between different branches. The numbers indicate the sequence in which successive bubbles join these branches. (e) to (h): Divergence angle as a function of bubble release sequence number for the corresponding cases shown in the top row. The red dashed lines show the averaged values. From left to right, the release periods are 100, 50, 42, and 36 ms, respectively.

mass center distance $\ell \lesssim d$, and is associated with significant bubble squeezing, deformation, and quick velocity changes. Whereas non-contact repulsion is effective when $\ell \gtrsim d$ and is less violent.

For the sake of clarity, in the following, the specific bubble that is focused on is named bubble 0. Other bubbles are labeled in chronological order of their release. Specifically, the two bubbles that rise to the free surface prior to bubble 0 are bubbles -2 and -1 , respectively. The one that follows it is called bubble 1.

B. Disordered and fixed two-armed modes

The disordered mode is seemingly the most common situation. It occurs when the bubble release period T is relatively large. This mode is characterized by random pair collisions between bubbles. For instance, as bubble -1 rises to the free surface, it collides with bubble -2 which is already at the emergence site. The two bubbles are knocked away by each other in opposite directions, creating a 180° divergence angle. By the time bubble 0 reaches the surface, the influence of the previous collision has vanished. Bubble 0 stays at the center and collides with the subsequent bubble 1, resulting in opposite emission directions that do not necessarily align with those of bubbles -2

and -1 . As a consequence, the divergence angle jumps between 180° and other random values (Fig. 4e). Additionally, a large T results in a relatively weak liquid jet, such that the bubbles tend to aggregate near the central region of the free surface. Both of these features hinder the formation of regular patterns with distinguishable numbers of arms.

The transition mechanism from the disordered mode to a fixed two-armed mode (Fig. 4b) is straightforward: When T is decreased below a certain threshold value, bubble -1 , after collision with bubble -2 , does not have enough time to move far away from the center before bubble 0 rises to the free surface. Consequently, bubble 0 collides with bubble -1 and bounces towards the opposite direction to the latter's position vector. Similarly, bubble 1 is emitted in the opposite direction to that of bubble 0 , following the path of bubble -1 . In this way, the bubbles alternatively join two branches with a constant divergence angle of $\varphi = 180^\circ$, as depicted in Fig. 4(f).

C. Multi-armed modes

The multi-armed modes occur when the bubble release period is further decreased. They exhibit richer phenomena compared with the disordered and fixed two-armed situations. Figs. 4(c) and 4(d) show a fixed five-armed pattern and a spiral three-armed pattern, respectively. A 3D view of a single bubble trajectory in the five-armed case is displayed in Fig. 5(a). The projection of this trajectory onto the horizontal plane is shown in Fig. 5(b) alongside the trajectories of two consecutive bubbles.

For patterns with fixed arms, the number n of arms is related to the divergence angle φ by

$$n\varphi = 2\pi m, \quad (5)$$

where m is a small integer. Without loss of generality, we assume φ is positive in Eq. (5). Eq. (5) states that the emissions of n successive bubbles sweep through exactly m complete circles. Evidently, consecutive bubbles do not necessarily go to adjacent arms. If Eq. (5) is only approximately satisfied, spiral patterns are observed. For example, with the averaged divergence angles shown in Figs. 4(g) and 4(h), the fixed five-armed mode corresponds to $5 \times 143.9^\circ \approx 360^\circ \times 2$, whereas the spiral three-armed mode corresponds to $3 \times 124.6^\circ \gtrsim 360^\circ \times 1$.

The twisted trajectories in Fig. 5 indicate complex bubble dynamics in the vicinity of the bubble emergence site. Yoshikawa *et al.* [24] note that, despite the arms may rotate, “the motion of each bubble is purely radial.” This is true except for in the short-period initial phase of the bubble

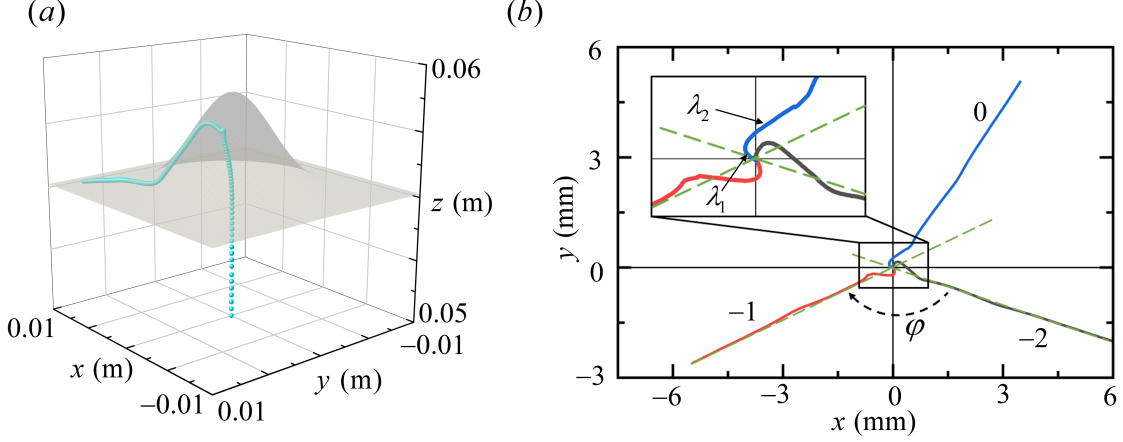


FIG. 5. (a) Free surface (gray) and trajectory (cyan) of a single bubble in a five-armed case. (b) Trajectories of three consecutive bubbles projected onto the horizontal plane. The green dashed lines indicate the emission directions of bubbles -2 and -1 .

motion, as can be seen in Fig. 5(b). In order to understand the entire process that determines the divergence angle, we divide the trajectory of a single bubble into six stages, labeled I to VI, in Fig. 6. The dynamics of the bubbles and their connection with the mechanisms listed in section III A are described in detail below.

Firstly, a significant difference between multi-armed modes and the simpler fixed two-armed mode is that the former cannot be explained solely by binary bubble collisions. This adds complexity to the analysis of the underlying physics, necessitating the inclusion of mechanism (ii), i.e., non-contact repulsion. This mechanism is illustrated in Fig. 7, where three snapshots of the three-armed situation are shown in chronological order. During this stage, bubble 0 is still rising below the free surface without colliding with preceding bubbles. Floating on the free surface with a short distance from the center where the bubbles emerge, bubble -2 acts as an obstacle that partially blocks the rightward motion of the liquid flow. As a consequence of this asymmetry, bubble 0's rising path is deflected to the left, as if it experiences repulsion from bubble -2 . Since there is no direct contact between bubbles 0 and -2 throughout the interaction, the horizontal displacement of bubble 0 from the central axis is mild. We denote this displacement by λ_1 . This process corresponds to stage I in Fig. 6(a). Similar interactions also occur between bubbles 0 and -1 . However, since bubble -1 is only slightly deviated from the center, its influence on bubble 0's horizontal motion is much weaker than the influence of bubble -2 . The repulsion from other floating bubbles is negligible due to their larger distance from bubble 0. Therefore, λ_1 is roughly in the opposite direction of

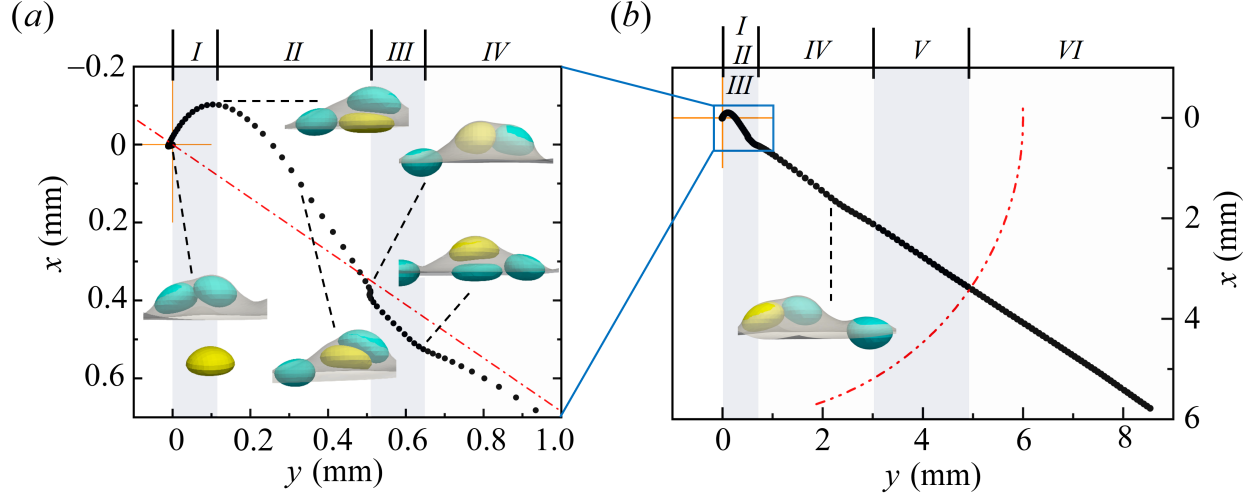


FIG. 6. Bubble 0's trajectory projected onto the horizontal plane. Black dots represent positions sampled with equal time intervals. The trajectory is divided into six stages, labeled on the top. Insets show the instantaneous position and shape of bubbles near the free surface (bubble 0 colored yellow). The dash-dotted line in panel (a) indicates the final emission direction of bubble 0. The arc in panel (b) marks the edge of the bump.

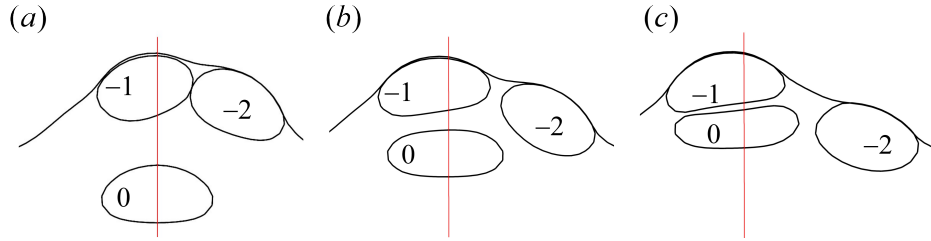


FIG. 7. Snapshots of the non-contact repulsion process between bubbles 0 and -2, taken in the cross section where the centers of the two bubbles are located. The red line shows the position of the central axis.

bubble -2's position vector in the horizontal plane, as shown in the inset of Fig. 5(b).

The motion of bubble 0 in stage II is governed by mechanism (i), i.e., pair collision. Fig. 8 depicts the collision process between bubbles 0 and -1 in the cross-section where the centers of the two bubbles are located. The snapshot in Fig. 8(a) is taken at about the same time as that in Fig. 7(c). When approaching the free surface, bubble 0 is impeded by bubble -1, squeezed and pushed away by it. During this process, bubble 0 acquires a horizontal displacement roughly in the opposite direction of bubble -1's position vector, which can also be observed in the inset of Fig. 5(b). We denote this displacement by λ_2 .

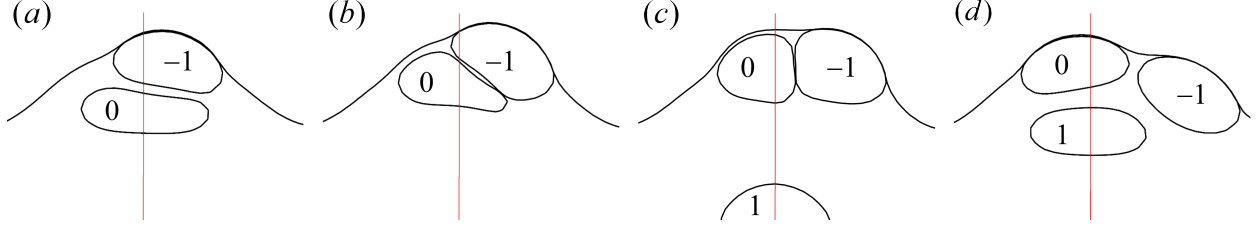


FIG. 8. Snapshots of the pair collision process between bubbles 0 and -1 , taken in the cross section where the centers of the two bubbles are located. The red line shows the position of the central axis.

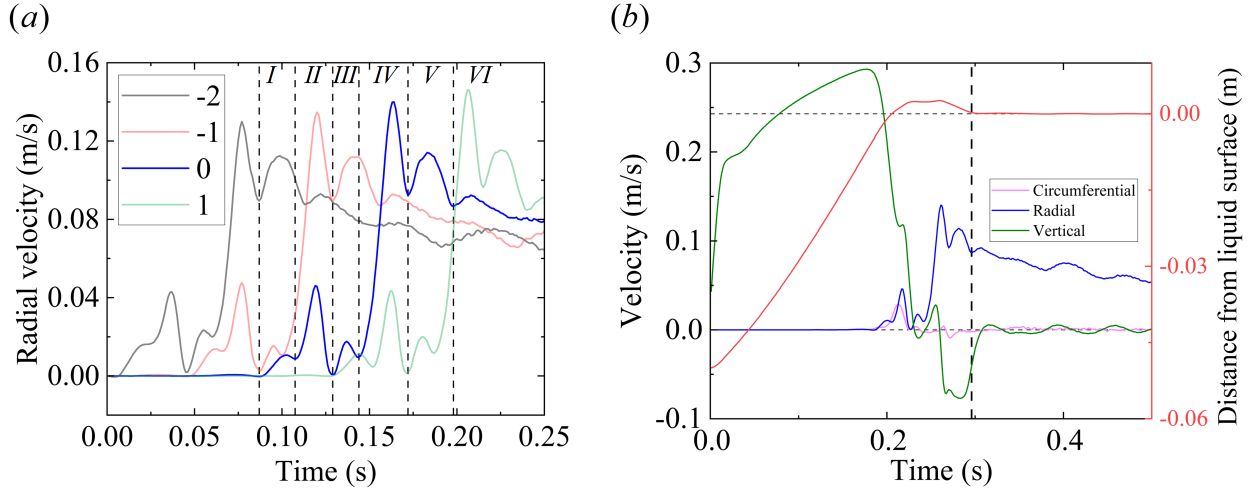


FIG. 9. (a) Radial velocity versus time for bubbles -2 , -1 , 0 , and 1 (from left to right). Stages are labeled with respect to bubble 0 . (b) Time dependence of bubble 0 's radial (blue), vertical (green), and circumferential (pink, clockwise positive) velocities. The red line represents the distance between the bubble mass center and the undisturbed free surface. Time is set to zero at the instant of bubble release.

Although mechanisms (i) and (ii) both have effects to accelerate bubble 0 , the bubble's radial velocity falls back to nearly zero by the end of stage II. This can be seen from Fig. 9(a), where the radial velocities of bubbles -2 , -1 , 0 , and 1 are shown as functions of time. The velocity variation can also be deduced from Fig. 6. In this figure, the dots in the trajectories are successively sampled from the numerical results with a constant time interval. Therefore, their sparseness is an indicator of the bubble's horizontal velocity magnitude. This deceleration of bubble 0 is due to mechanism (iii) mentioned in section III A, i.e., the confinement of the bump. As revealed in Fig. 8(c), after collision with bubble -1 , bubble 0 is located in the very top region of the bump. Thus, its horizontal motion is restricted by the capillary effect of the deformed and more vertical side surface of the bump.

It is noteworthy that, up to this point, the bubble's displacement from the central axis is no greater than half its radius. However, according to Fig. 6(a), the final emission direction (the red dash-dotted line) of bubble 0 has been essentially determined. All the remaining stages play a role to “launch” this nearly stationary bubble and transport it in the same direction as its current position vector.

The collision with bubble 0 also promotes bubble -1 to leave the central region. As a consequence, bubble 0 has more room to flatten, and the bump surface becomes less steep. This relieves the constraint imposed by the bump, allowing bubble 0 to regain a small velocity away from the center advected by the radial flow mentioned earlier. This process corresponds to stage III in Figs. 6 and 9(a).

Stage IV is characterized by the pair collision between bubbles 0 and 1, which continues to accelerate bubble 0. The radial velocity of bubble 0 rapidly reaches its maximum value over the entire bubble motion, followed by a short period of deceleration caused again by the confinement of the deformed bump. The instantaneous configuration is similar to that shown in Fig. 8(c), but with bubble numbers -1 and 0 replaced by 0 and 1, respectively.

Being pushed away from the center by bubble 1, the subsequent motion of bubble 0 in stage V is driven by the divergent radial flow (mechanism (iv) in section III A). This effect of flow advection is demonstrated by the streamlines shown in Fig. 10(a). The bubble continues moving within the bump until it encounters the edge of it, where the bubble experiences a temporary deceleration due to the transition between the bumped and horizontal free surface. This reason can be deduced from Fig. 9(b), where the vertical dashed line indicates that the local minimum radial velocity occurs exactly when the bubble reaches the flat liquid surface from a higher elevation.

After escaping from the bump, in stage VI, bubble 0 assumes a purely radial motion, as evidenced by the negligible circumferential velocity shown in Fig. 9(b). According to the contour lines in Fig. 10(b), the radial velocity of the bubbles is smaller than that of the surrounding liquid, revealing that the bubbles are passively advected by the radial liquid flow in the surface layer. During this stage, both the radial and vertical velocity components of the bubble undergo mild fluctuations over time, as shown in Fig. 9(b). These fluctuations are likely caused by the outward-propagating annular surface waves faintly visible in the top row of Fig. 4. Due to volume conservation and viscous dissipation, the radial flow weakens with increasing radius. The bubbles gradually decelerate and eventually stop at some distance from the center.

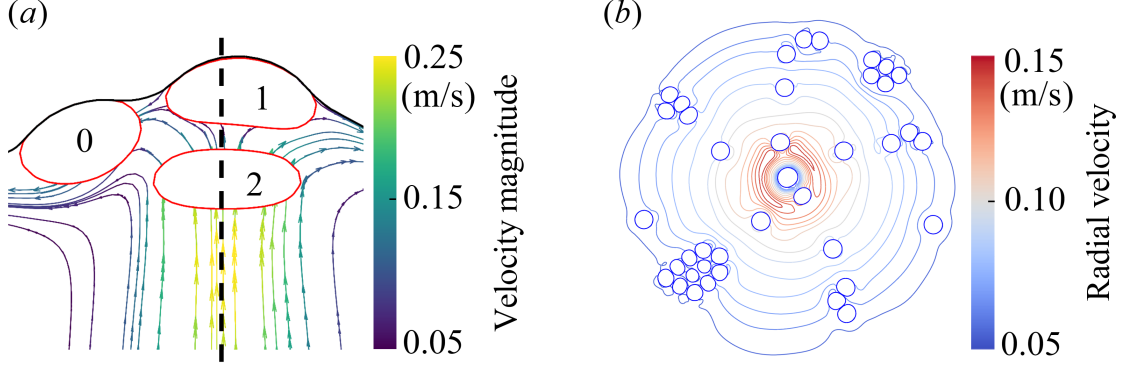


FIG. 10. (a) Snapshot of a cross-sectional view of the bubbles near the bump. The streamlines are colored according to the velocity magnitude. The dashed line indicates the central axis. (b) Contour lines of the liquid's radial velocity in a horizontal plane slightly below the free surface. The small circles are bubbles floating on the surface.

IV. FURTHER THEORETICAL CONSIDERATIONS

We propose a simple model to describe the dependence of the divergence angle φ on the bubble release period T , provided that all other parameters are fixed. Without loss of generality, we assume the motion of bubble -2 is in the direction of $-x$, as illustrated in Fig. 11(a). Based on the discussions in section III C, in stages I and II, the motion of bubble 0 is mainly influenced by bubbles -2 and -1 , with the displacements occurring in the opposite directions of these two bubbles. Therefore, λ_1 and λ_2 are plotted in Fig. 11(a) parallel to the reverse extensions of the two bubbles' position vectors. In later stages, bubble 0 is launched in the direction of the vector sum of λ_1 and λ_2 . In order that the successive bubbles form a regular pattern, the angles between bubbles 0 and -1 and between bubbles -1 and -2 are both φ . With introduction of the variable $\alpha = \varphi - \pi/2$, one obtains $\beta = \pi/2 - 2\alpha$, where β is defined in Fig. 11(a). Denoting the magnitude of λ_1 and λ_2 by λ_1 and λ_2 , respectively, the geometric constraint requires $\tan \beta = (\lambda_1 - \lambda_2 \sin \alpha) / (\lambda_2 \cos \alpha)$, which yields

$$\varphi = \frac{\pi}{2} + \arcsin \frac{\lambda_2}{2\lambda_1}. \quad (6)$$

When $\lambda_2/\lambda_1 \rightarrow 2^-$, $\varphi \rightarrow \pi$, corresponding to the two-armed mode limit. When $\lambda_2/\lambda_1 \rightarrow 0^+$, $\varphi \rightarrow \pi/2$, indicating a four-armed mode. However, this latter situation is unlikely to occur because of the fact that while λ_2 is finite in general, λ_1 , caused by non-contact repulsion, cannot be excessively large. The situation of $\lambda_2/\lambda_1 > 2$ is not covered by Eq. (6), either can it be described

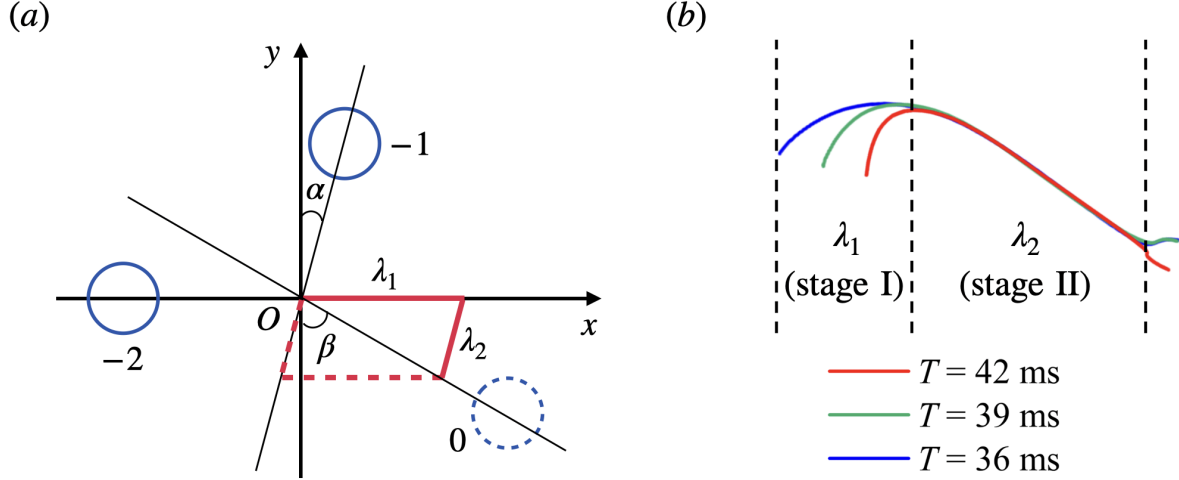


FIG. 11. (a) Geometric configuration of bubbles on the free surface (bubble size and position for illustrative purposes only). (b) Simulated bubble trajectories projected onto the horizontal plane with appropriate translation and rotation.

by the geometrical configuration shown in Fig. 11(a). Actually, it represents the scenario that the non-contact repulsion between bubbles -2 and 0 is too small to influence the pattern formation, and the divergence angle is dominated by the pair collision between bubbles -1 and 0 . Thus, the fixed two-armed mode or disorder mode is expected.

It is useful to further relate λ_1 and λ_2 to the release period T . The two displacements for three cases with different T are shown in Fig. 11(b) after appropriate translation and rotation within the horizontal plane. It is noteworthy that, while λ_1 varies, λ_2 is nearly the same for all the three cases. This is because λ_2 is caused by the pair collision within the bump. The strong effects of squeezing and bump confinement render λ_2 dominated by geometric factors such as the bubble and bump sizes. Therefore, it is reasonable to consider λ_2 as a constant that is independent of T . On the other hand, λ_1 , which results from non-contact repulsion, is expected to be inversely related to the average distance between bubbles 0 and -2 as bubble 0 approaches the free surface. This distance, in turn, is positively correlated with T . Based on this analysis, a very simple relation between λ_1 and T is proposed as $\lambda_1 \propto 1/(aT - b)$, where the coefficients a and b may depend on parameters such as the bubble size, liquid viscosity, and surface tension coefficient. This relation can be substituted into Eq. (6) while keeping λ_2 constant. After including the fixed two-armed

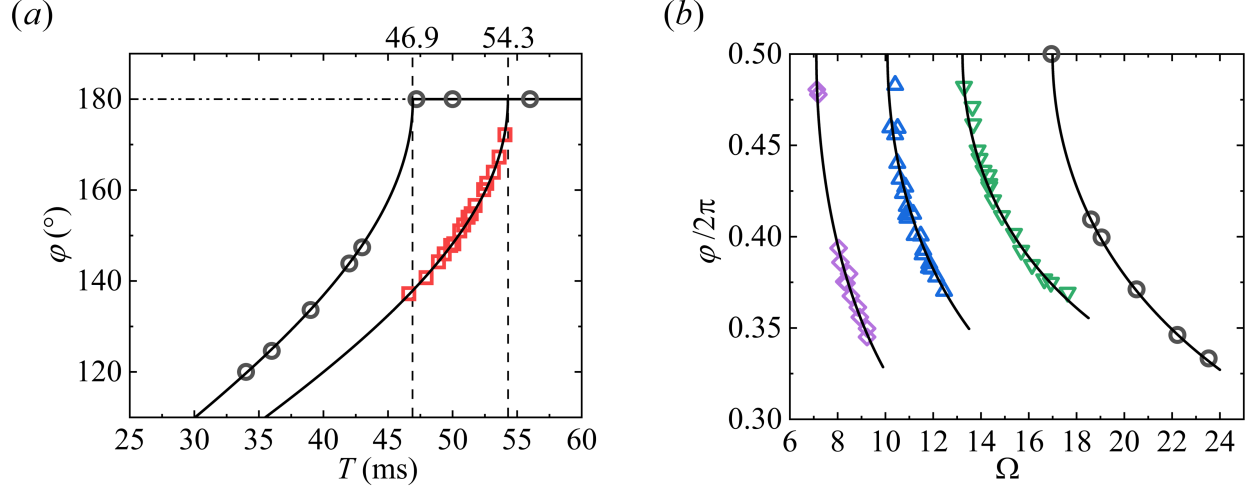


FIG. 12. (a) Divergence angle φ versus release period T . Red squares denote experimental data extracted from Fig. 1.2(a) in Ref. [26], with $Oh \approx 0.099$ and $Bo = 17$. (b) Divergence angle versus dimensionless frequency Ω . The three data sets on the left are experimental results extracted from Fig. 5(a) in Ref. [24]. From left to right, the Ohnesorge and Bond numbers, estimated based on the available information in Ref. [24], are approximately 0.26 and 23, 0.21 and 18, 0.11 and 11, respectively. In both panels, the present numerical results are denoted by black circles; solid curves represent predictions using Eq. (7) or (8).

mode situation, the model is expressed as

$$\varphi = \begin{cases} \frac{\pi}{2} + \arcsin(aT - b), & T \leq \frac{b+1}{a}, \\ \pi, & T > \frac{b+1}{a}. \end{cases} \quad (7)$$

Eq. (7) is valid unless T is too large, in which case disordered, instead of regular, patterns, will be observed. Fig. 12(a) shows the averaged φ as a function of T for eight simulation cases (black circles) and the experimental data from Ref. [26] (red squares). Notably, with a and b fitted for each data set, the predictions of Eq. (7) (solid lines) have a remarkable consistency with both the numerical and experimental results. The fitted coefficients for the two curves, from left to right, are $a = 0.039 \text{ ms}^{-1}$, $b = 0.83$, and $a = 0.035 \text{ ms}^{-1}$, $b = 0.90$, respectively.

Eq. (7) can be rewritten in dimensionless form as:

$$\frac{\varphi}{2\pi} = \begin{cases} \frac{1}{4} + \frac{1}{2\pi} \arcsin\left(\frac{A}{\Omega} - b\right), & \Omega \geq \frac{A}{b+1}, \\ \frac{1}{2}, & \Omega < \frac{A}{b+1}, \end{cases} \quad (8)$$

where $\Omega = \rho_l d^2 / (\mu_l T)$ is the dimensionless bubble release frequency defined in Ref. [24]. Correspondingly, $A = \rho_l d^2 a / \mu_l$. The dependence of $\varphi/(2\pi)$ on Ω is shown in Fig. 12(b). The

present numerical results are still denoted by black circles. The other three data sets correspond to experimental data extracted from Fig. 5(a) in Ref. [24]. The results of the theoretical model Eq. (8) are shown as black curves with A and b fitted for each set of data. The values of A and b for the four curves in Fig. 12(b), from left to right, are: 13.3 and 0.87, 16.5 and 0.64, 17.9 and 0.35, 31.1 and 0.83, respectively. Good agreement is observed between the theoretical predictions and all the data sets.

In the following, we consider the possibility of observing different multi-armed patterns in reality. Fig. 13(a) shows the number n of arms that is expected to be seen as the release period T varies. This mapping is obtained by calculating the corresponding φ at a given T using Eq. (7), then finding n within the range $2 \leq n \leq 15$ that best fits Eq. (5) with all possible m . The upper bound of 15 is set considering that for very large n , the finite-sized bubbles are so crowded that the arms become difficult to distinguish in practice. It can be seen from Fig. 13(a) that each n may correspond to several discontinuous intervals of T . The accumulated range of T for a given n is shown in Fig. 13(b). The probability of appearances of n -armed mode can thus be estimated based on the height of the bars.

According to Fig. 13, a six-armed mode seldom exists. In addition, due to the reason discussed earlier, situations near the left edge of Fig. 13(a) ($\varphi \gtrsim 90^\circ$ with $\lambda_2/\lambda_1 \rightarrow 0^+$) cease to be possible, reducing the possibility of $n = 4, 7, 11$, etc. The above analyses align well with our experience that the three- and five-armed patterns are easier to achieve than other multi-armed modes by adjusting the period T in the numerical simulations.

V. SUMMARY AND CONCLUSIONS

This work elucidates the formation mechanism of regular surface patterns induced by chains of small rising bubbles. Direct numerical simulations reveal how distinct morphologies stem from non-contact bubble repulsion, pair collisions, free-surface deformation, and ambient flow advection. We establish a theoretical model relating the number of pattern arms to the bubble release period, showing quantitative agreement with both simulation data and experimental results from the literature. Future studies should explore other parameters including liquid viscosity, surface tension coefficient, and bubble diameter.

A key feature of the regular patterns is the lateral dispersion—instead of aggregation—of surface bubbles. This suggests potential applications in interfacial heat transfer enhancement via foam

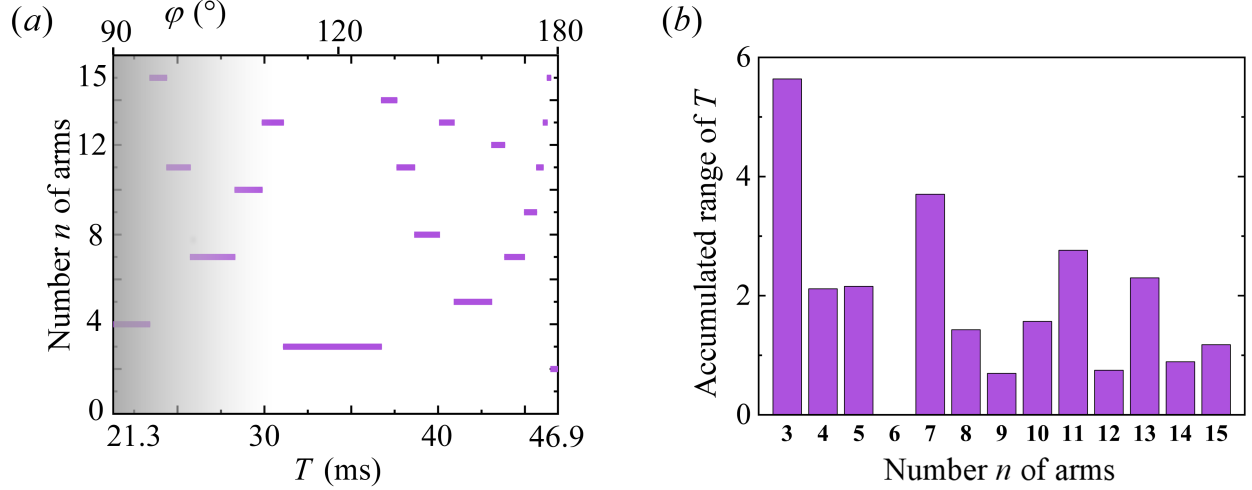


FIG. 13. (a) Number of observed arms estimated using Eq. (7) (with $a = 0.039 \text{ ms}^{-1}$ and $b = 0.83$) and Eq. (5) as a function of bubble release period T . Cases in the gray area are unlikely to occur. (b) Accumulated range of T within which n -armed mode can be observed.

suppression and contaminant removal through spiral-pattern-driven surface sweeping. Moreover, the patterns' sensitivity to operational parameters enables real-time monitoring of gas flow rates, bubble release intervals, and fluid properties. As a minimal model of self-organization, this study demonstrates how localized dynamics govern emergent macroscopic order, offering insights for understanding, designing, and controlling collective behaviors in broader self-organized systems.

ACKNOWLEDGEMENTS

D. Li and G. Zhou acknowledge the support of the National Natural Science Foundation of China (grant number 12202441). D. Li appreciates the advice from Dr. Petr Karnakov on the use of Aphros. The authors also thank Dr. Zibo Ren for his participation in the early stage of this study.

* zgzh@ucas.ac.cn

- [1] A. A. Kulkarni and J. B. Joshi, Bubble formation and bubble rise velocity in gas-liquid systems: a review, *Ind. Eng. Chem. Res.* **44**, 5873–5931 (2005).
- [2] S. Takagi and Y. Matsumoto, Surfactant effects on bubble motion and bubbly flows, *Annu. Rev. Fluid Mech.* **43**, 615–636 (2011).
- [3] Y. Tagawa, I. Roghair, V. N. Prakash, M. van Sint Annaland, H. Kuipers, C. Sun, and D. Lohse, The

- clustering morphology of freely rising deformable bubbles, *J. Fluid Mech.* **721**, R2 (2013).
- [4] D. Lohse, Bubble puzzles: from fundamentals to applications, *Phys. Rev. Fluids* **3**, 110504 (2018).
- [5] F. Risso, Agitation, mixing, and transfers induced by bubbles, *Annu. Rev. Fluid Mech.* **50**, 25–48 (2018).
- [6] F. Raymond and J. M. Rosant, A numerical and experimental study of the terminal velocity and shape of bubbles in viscous liquids, *Chem. Eng. Sci.* **55**, 943–955 (2000).
- [7] B. Yang, A. Prosperetti, and S. Takagi, The transient rise of a bubble subject to shape or volume changes, *Phys. Fluids* **15**, 2640–2648 (2003).
- [8] M. K. Tripathi, K. C. Sahu, and R. Govindarajan, Dynamics of an initially spherical bubble rising in quiescent liquid, *Nat. Commun.* **6**, 6268 (2015).
- [9] A. W. G. de Vries, A. Biesheuvel, and L. van Wijngaarden, Notes on the path and wake of a gas bubble rising in pure water, *Int. J. Multiphase Flow* **28**, 1823–1835 (2002).
- [10] G. Mougin and J. Magnaudet, Path instability of a rising bubble, *Phys. Rev. Lett.* **88**, 014502 (2001).
- [11] W. L. Shew and J. F. Pinton, Dynamical model of bubble path instability, *Phys. Rev. Lett.* **97**, 144508 (2006).
- [12] P. Ern, F. Risso, D. Fabre, and J. Magnaudet, Wake-induced oscillatory paths of bodies freely rising or falling in fluids, *Annu. Rev. Fluid Mech.* **44**, 97–121 (2012).
- [13] C. H. Marks, Measurements of the terminal velocity of bubbles rising in a chain, *J. Fluids Eng.* **95**, 17–22 (1973).
- [14] J. Zhang and L. S. Fan, On the rise velocity of an interactive bubble in liquids, *Chem. Eng. J.* **92**, 169–176 (2003).
- [15] B. Wang and S. A. Socolofsky, On the bubble rise velocity of a continually released bubble chain in still water and with crossflow, *Phys. Fluids* **27**, 103301 (2015).
- [16] O. Atasi, M. Ravisankar, D. Legendre, and R. Zenit, Presence of surfactants controls the stability of bubble chains in carbonated drinks, *Phys. Rev. Fluids* **8**, 053601 (2023).
- [17] H. Lhuissier and E. Villermaux, Bursting bubble aerosols, *J. Fluid Mech.* **696**, 5–44 (2012).
- [18] E. Ghabache and T. Séon, Size of the top jet drop produced by bubble bursting, *Phys. Rev. Fluids* **1**, 051901 (2016).
- [19] L. Deike, E. Ghabache, G. Liger-Belair, A. K. Das, S. Zaleski, S. Popinet, and T. Séon, Dynamics of jets produced by bursting bubbles, *Phys. Rev. Fluids* **3**, 013603 (2018).
- [20] J. M. Gordillo and J. Rodríguez-Rodríguez, Capillary waves control the ejection of bubble bursting

- jets, *J. Fluid Mech.* **867**, 556–571 (2019).
- [21] S. Poulain, E. Villiermaux, and L. Bourouiba, Ageing and burst of surface bubbles, *J. Fluid Mech.* **851**, 636–671 (2018).
 - [22] J. Feng, M. Muradoglu, H. Kim, J. T. Ault, and H. A. Stone, Dynamics of a bubble bouncing at a liquid/liquid/gas interface, *J. Fluid Mech.* **807**, 324–352 (2016).
 - [23] J. H. Guan, S. I. Tamim, C. W. Magoon, H. A. Stone, and P. J. Sáenz, Galloping bubbles, *Nat. Commun.* **16**, 1572 (2025).
 - [24] H. N. Yoshikawa, C. Mathis, P. Maissa, G. Rousseaux, and S. Douady, Pattern formation in bubbles emerging periodically from a liquid free surface, *Eur. Phys. J. E.* **33**, 11–18 (2010).
 - [25] S. Douady and Y. Couder, Phyllotaxis as a physical self-organized growth process, *Phys. Rev. Lett.* **68**, 2098–2101 (1992).
 - [26] H. N. Yoshikawa, C. Mathis, P. Maissa, and G. Rousseaux, Spiral pattern formation in a simple two-phase flow system, in *Proceedings of the Conference on Chaos, Complexity and Transport* (Marseille, France, 2012) p. 113–122.
 - [27] P. Karnakov, S. Litvinov, and P. Koumoutsakos, Computing foaming flows across scales: From breaking waves to microfluidics, *Sci. Adv.* **8**, eabm0590 (2022).
 - [28] J. B. Bell, P. Colella, and H. M. Glaz, A second-order projection method for the incompressible Navier-Stokes equations, *J. Comput. Phys.* **85**, 257–283 (1989).
 - [29] R. Scardovelli and S. Zaleski, Analytical relations connecting linear interfaces and volume fractions in rectangular grids, *J. Comput. Phys.* **164**, 228–237 (2000).
 - [30] P. Karnakov, S. Litvinov, and P. Koumoutsakos, A hybrid particle volume-of-fluid method for curvature estimation in multiphase flows, *Int. J. Multiphase Flow* **125**, 103209 (2020).